**High sensitivity near-infrared imaging of fluorescent nanosensors**

*Julia Ackermann, Jan Stegemann, Tim Smola, Eline Reger, Sebastian Jung, Anne Schmitz, Svenja Herbertz, Luise Erpenbeck, Karsten Seidl, Sebastian Kruss**

J. Ackermann, T. Smola, E. Reger
Fraunhofer Institute for Microelectronic Circuits and Systems, Finkenstrasse 61, 47057 Duisburg, Germany
Department EBS, University Duisburg-Essen, Bismarkstrasse 81, 47057 Duisburg, Germany

J. Stegemann
Fraunhofer Institute for Microelectronic Circuits and Systems, Finkenstrasse 61, 47057 Duisburg, Germany
Department of Chemistry, Ruhr-University Bochum, Universitätstrasse 150, 44801 Bochum, Germany

S. Jung
ZEMOS Center for Solvation Science, Ruhr-University Bochum, Universitätstrasse 150, 44801 Bochum, Germany

A. Schmitz, L. Erpenbeck
Department of Dermatology, University Hospital Münster, Von-Esmarch-Strasse 58, 48149 Münster, Germany

S. Herbertz
Fraunhofer Institute for Microelectronic Circuits and Systems, Finkenstrasse 61, 47057 Duisburg, Germany

K. Seidl
Fraunhofer Institute for Microelectronic Circuits and Systems, Finkenstrasse 61, 47057 Duisburg, Germany
Department EBS, University Duisburg-Essen, Bismarkstrasse 81, 47057 Duisburg, Germany
Center for Nanointegration Duisburg-Essen (CENIDE), Carl-Benz-Strasse 199, 47057 Duisburg, Germany

S. Kruss
Fraunhofer Institute for Microelectronic Circuits and Systems, Finkenstrasse 61, 47057 Duisburg, Germany
Department of Chemistry, Ruhr-University Bochum, Universitätstrasse 150, 44801 Bochum, Germany
Center for Nanointegration Duisburg-Essen (CENIDE), Carl-Benz-Strasse 199, 47057 Duisburg, Germany
E-mail: sebastian.kruss@rub.de

Keywords: near-infrared fluorescence, imaging, biosensors, carbon nanotubes, dopamine

Biochemical processes are fast and occur on small length scales, which makes them difficult to measure. Optical nanosensors based on single-wall carbon nanotubes (SWCNTs) are able to capture such dynamics. They fluoresce in the near-infrared (NIR, 850 – 1700 nm) tissue transparency window and the emission wavelength depends on their chirality. However, NIR imaging requires specialized and cooled InGaAs cameras with low resolution because the quantum yield of normal Si-based cameras rapidly decreases in the NIR. Here, we developed an efficient one-step phase separation approach to isolate monochiral (6,4)-SWCNTs (880 nm emission) from mixed SWCNT samples. It enabled us to image them in the NIR with high-resolution standard Si-based cameras (>50 x more pixels). (6,4)-SWCNTs modified with $(GT)_{10}$-ssDNA become highly sensitive for the important neurotransmitter dopamine. These sensors are 1.7-fold brighter and 7.5 x more sensitive and allow fast imaging (< 50 ms). They enable high-resolution imaging of dopamine release from cells. Thus, the assembly of biosensors from (6,4)-SWCNTs combines the advantages of nanosensors working in the NIR with the sensitivity of (Si-based) cameras and enables broad usage of these nanomaterials.

## 1. Introduction

Cells use biomolecules to transmit information. This communication occurs in waves of biomolecules from a transmitter cell through the extracellular space to other (receiver) cells. This type of signal transmission takes place in many biological situations such as the communication of neurons[1] *via* the release of neurotransmitters or in cells of the immune system[2], which form reactive oxygen and nitrogen species in inflammatory processes to destroy microorganisms. The concentration of the released substances changes spatially and temporally and is a biochemical fingerprint of the biological state. However, such biologically relevant processes occur on temporal (ms) and spatial (nm) scales that are difficult to access using established methods.[3] For example, electrochemical methods such as amperometry or voltammetry lack the required spatial resolution determined by the number of electrodes and are invasive as the microelectrodes penetrate the tissue.[4] On the other hand optical methods provide often only indirect information e.g. by labeling cellular components[5,6] or suffer from photobleaching.[7]

In this context, nanomaterials such as single-wall carbon nanotubes (SWCNTs) have emerged as promising building blocks to capture these dynamics.[3,8] In addition to a high surface-to-volume ratio that makes them sensitive to single-molecule detection[9–12], their surface can be chemically tailored[13–17]. Thus, SWCNTs have already been used for several bioimaging studies[18,19] and the detection of numerous analytes such as reactive oxygen species[20–23], small molecules like nitroaromatics[24,25] or neurotransmitters[26,27], proteins[28–30], sugars[31], enzymes[32] or bacteria[33]. Due to their fluorescence in the near-infrared (NIR, 850 – 1700 nm), which shows no bleaching or blinking, they represent stable fluorophores, whose emission falls within the biological transparency window[34]. Here, reduced scattering and autofluorescence of biological samples allow for increased signal-to-noise ratios (SNR) during detection[35].

Recently their outstanding potential in detecting the cellular release of the neurotransmitters dopamine[36–38] and serotonin[39] was demonstrated with an unprecedented high spatiotemporal resolution, which also allowed observation of dopamine release from over 100 dopaminergic varicosities simultaneously.

However, one major drawback for scientists wishing to use such fluorphores is that a specialized NIR detector is required. NIR emission is usually collected with indium gallium arsenide (InGaAs) detectors. Their fabrication process is complex, the resolution in terms of absolute pixel numbers is low, and the sensor must be cooled, for example with liquid nitrogen to reduce the high dark current.[35,40] This makes these cameras impractical and expensive (> 40,000 €) compared to the widely used Silicon (Si) cameras, which have a rapidly decreasing sensitivity in the NIR and have therefore problems to detect signals > 950 nm.[41,42]

The exact fluorescence wavelength of SWCNTs depends on their chirality (n,m).[43] (6,4)-SWCNTs, which are the species emitting closest to visible light with emission around 880 nm, would be well-suited for detection with commercial Si cameras while still taking advantage of the NIR. However, (6,4)-SWCNTs are not yet available in their pure form.

In general, the fabrication of sensors based on SWCNTs has so far been mainly based on mixtures of different chiralities, as the synthesis of pure species has not yet been performed on larger scales[44]. Advances in synthesis have led to the preparation of chirality-enriched SWCNT samples[45–47], as a result of which (6,5)-enriched CoMoCAT-SWCNTs with the main emission around 985 nm are already commercially available. Recently, they have been used for detection with Si cameras.[48,49] Although CoMoCAT-SWCNTs also contain some amount of (6,4)-SWCNTs, the sensitivity in combination with Si detectors is not as good because high concentrations have to be used that lead to quenching.[50] Xu et al. succeeded for the first time in preparing preferably (6,4)-SWCNTs with a purity of ~57% by adjusting the oxidation state

of the cobalt catalyst.[51] However, as long as high-purity SWCNTs are not yet commercially available, post-growth separation based on solution sorting techniques will remain a focus.[52] Here, various methods such as density gradient ultracentrifugation[53,54], ion-exchange[55] or gel column chromatography[56,57], enrichment over polymers[58–60], and aqueous two-phase extraction (ATPE)[61,62] have become established in recent years. ATPE, in particular, has proven to be fast, selective, cost-effective, and easily scalable. This method is usually based on two polymers, dextran and polyethylene glycol (PEG), added in a ratio where they are immiscible and thus form two phases.[63] SWCNTs are then dispersed using surfactants such as sodium deoxycholate (DOC), sodium cholate (SC), or sodium dodecyl sulfate (SDS), whereby separation is driven between the two phases by the properties of the resulting surfactant phase at the SWCNT surface, and then based on the exchange of phases of unwanted SWCNT chiralities for empty phases.[64] Li et al. recently published a simple pH-controlled method that separated (6,4)-SWCNTs and ten other species.[65] Subsequently, Nißler et al. used this method for chirality-pure sensors for the detection of various small molecules and also ratiometric sensing with different wavelengths.[66] Furthermore, Antaris et al. used (6,4)-SWCNTs obtained from density gradient ultracentrifugation in combination with Si-detectors for immunohistochemical staining of cells and cancer tissue sections.[67]

Surprisingly, sensing with (6,4)-SWCNTs using low-cost Si cameras has not yet been demonstrated. This is likely because a fast method for large-scale extraction of (6,4)-SWCNTs has been missing so far, as well as a simple process for subsequent SWCNT functionalization to tailor their surface chemistry.[52,66] Routes for easy exchange have now been developed, such as methanol-assisted surfactant exchange[68] or dialysis[52], leaving the obstacle of a rapid process for (6,4)-SWCNT extraction to make this material accessible to the broader community.

Here, we address this challenge and separate (6,4)-SWCNTs (emission at 880 nm) from commercial SWCNT mixtures ((6,5)-enriched CoMoCAT-SWCNTs) by tailoring an ATPE

protocol[65] to obtain (6,4)-SWCNTs for the first time quickly and easily scalable in only one single step. By replacing the surfactant shell around the SWCNTs with $(GT)_{10}$-single-stranded(ss)DNA sequences, we tailor these SWCNTs exemplarily as dopamine sensors. Hereby the optimum between detection with standard Si cameras and the use of NIR fluorescence imaging is achieved. We investigate the detection efficiency of these (6,4)-SWCNTs compared to the parental SWCNT mixture with both Si and InGaAs detectors. Finally, we demonstrate sensing of cellular dopamine release with high spatiotemporal resolution using standard microscope equipment (***Figure 1***). This method thus makes SWCNT-based nanosensors or labels accessible for a much larger community.

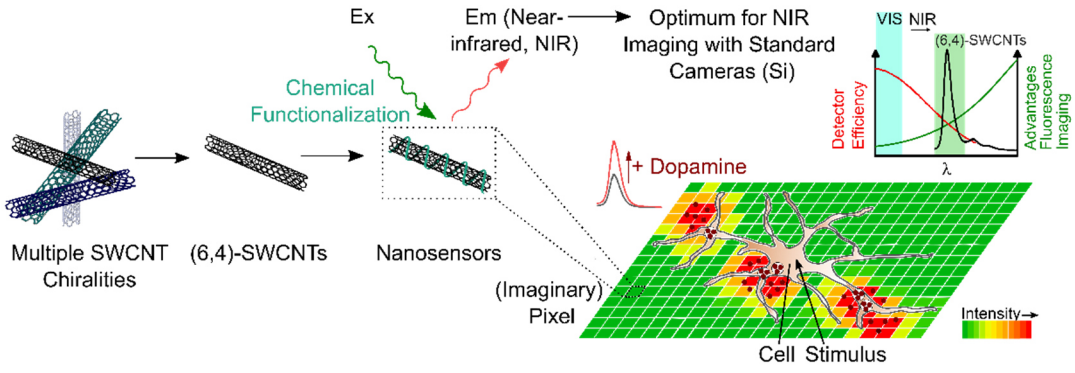


***Figure 1. High sensitivity NIR imaging of molecular sensors.*** *NIR fluorescent monochiral (6,4)-SWCNTs separated via aqueous two-phase extraction (ATPE) from standard SWCNT samples with multiple chiralities are used to visualize biomolecules such as the neurotransmitter dopamine. Their emission is in the sweet spot between high camera quantum yields of high-resolution and cost-effective (Si-based) cameras and the increasing advantages of the NIR (reduced scattering, autofluorescence). These sensors are rendered sensitive to dopamine by a specific surface functionalization with ssDNA. The nanosensors are immobilized on a glass surface and dopamine-releasing cells are cultured on top. Upon stimulation, the sensors acting as imaginary pixels report the release of dopamine by a fluorescence increase.*

## 2. Results and Discussion

### 2.1. (6,4)-SWCNT separation and optical characterization

To shift the overall SWCNT emission closer to the visible wavelength region, (6,4)-SWCNTs as the shortest SWCNT NIR emitter need to be separated from commercially available mixtures containing multiple chiralities. We decided to use ATPE as a scalable separation approach and used a pH-driven protocol.[65] The original protocol used a two-step separation with a mixture of 0.025% DOC, 0.05% SDS, and 0.5% SC but we did not get reproducible results. In the first step, pH-driven separation of (6,4)-SWCNTs from the remaining semiconducting SWCNTs should be performed, in which the (6,4)-SWCNTs accumulated together with metallic SWCNTs in the dextran-rich bottom phase. However, we were unable to separate (6,4)-SWCNTs from semiconducting (7,3)-SWCNTs with this mixture, despite testing different additions of hydrochloric acid (HCl, ***Figure S1*** a). This is mainly because these two SWCNT chiralities are difficult to separate due to their extremely similar diameters.[65] In addition, even slight variations in surfactant conditions can lead to altered experimental results.

Therefore, we modified it accordingly and finally developed a protocol achieving single-chirality (6,4)-SWCNTs in only one step, which makes it simple to reproduce and to scale up (***Figure 2*** a). Since SC is known to have a chirality dependent affinity[65], we systematically increased the SC content within this mixture and found that an increase in SC content (0.6 – 0.9% SC tested) lead to an optimized separation of (6,4)- and (7,3)-SWCNTs at 0.7% SC and higher (***Figure S1*** b -e). It was noticeable that with increasing SC concentration, higher amounts of HCl addition were required to separate the (6,4)- from the (7,3)-SWCNTs (***Figure S1*** f). For subsequent experiments, the SC content of 0.7% with lower HCl addition was chosen because, on the one hand, the risk of surfactant flocculation and thus SWCNT precipitation rises with an increasingly acidic environment, and, on the other hand, the peak ratio of (6,4)-/(7,3)-SWCNTs was highest.

After finding the optimal surfactant conditions, the second separation step of the published protocol was followed, which consisted of the addition of sodium hypochlorite (NaClO), which is known to separate metallic from semiconducting SWCNTs.[65] Here, we found that after increasing the SC content to 0.7%, the addition of NaClO caused the separation of (6,4)-SWCNTs into the dextran-rich bottom phase (instead of the PEG-rich top phase at 0.5% SC content), whereas metallic SWCNTs migrated mostly into the interfacial layer and the PEG-rich top phase (***Figure S2*** a-e). Furthermore, the addition of NaClO further improved the peak ratio of (6,4)/(7,3)-SWCNTs and based on the absorbance spectrum of the final bottom phase (***Figure S2*** d) nearly all peaks could be assigned to (6,4)-SWCNTs. The two large peaks at 586 nm and 885 nm correspond to the $E_{22}$ and $E_{11}$ excitonic transitions of (6,4)-SWCNTs, while the peak at 414 nm could result from incomplete separation of metallic SWCNTs as the $E_{33}$ transition is located at wavelengths < 400 nm and the peak intensity further decreased after metallic separation. The small peaks at 534 nm and 773 nm are known to be phonon sidebands of (6,4)-SWCNTs.[43,69,70] Based on fitting all semiconducting chiralities present in the starting material compared to the final bottom phase and comparing the resulting area of each peak assuming simplified the same absorption cross section for all SWCNTs, the purity of the material thus improved from 9.4 % containing (6,4)-SWCNTs to > 95% (***Figure S2*** a, d).

Since in the optimized surfactant mixture (6,4)-SWCNTs remained in the bottom phase after metallic separation and did not migrate into the top phase, the next step was to test whether the two-step separation procedure could be reduced to a one-step separation by the simultaneous addition of HCl and NaClO at the beginning. Interestingly, based on characterization *via* absorption spectra, this led to the same but faster result and pure (6,4)-SWCNTs remained in the bottom phase (***Figure S2*** f). As a result, this process also did not require a mimic phase and we were able to extract large amounts of (6,4)-SWCNTs (***Figure 2*** a). To further confirm the purity of the (6,4)-SWCNTs, 2D excitation-emission plots were acquired before (CoMoCAT-

SWCNTs) and after phase separation, in which the individual chiralities can be uniquely assigned based on their associated transitions (***Figure 2*** b). It is evident that the main emission at 980 nm, originating from the (6,5)-enriched CoMoCAT-SWCNTs, shifted after phase separation to the (6,4)-SWCNT emission around 880 nm. In addition, there is a very weak emission at 985 nm, which is identical in emission to that of (6,5)-SWCNTs. However, the excitation wavelength shifted from 567 nm to 580 nm and therefore it is more likely that this feature corresponds to the phonon sideband of (6,4)-SWCNTs.[69]

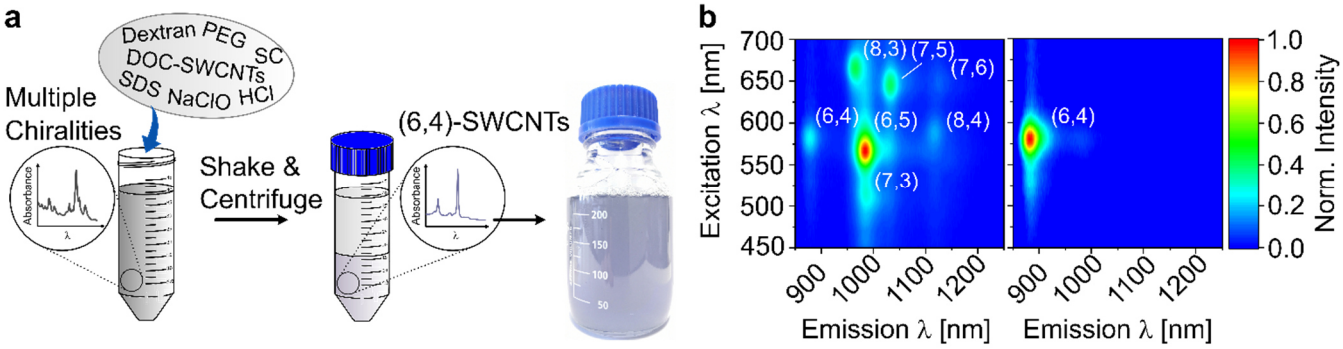


***Figure 2. One-step large-scale isolation of (6,4)-SWCNTs.*** *a) One-step aqueous two-phase extraction is used to isolate (6,4)-SWCNTs from other chiralities, providing a highly scalable approach. b) 2D excitation-emission plot before (CoMoCAT-SWCNTs) and after phase separation ((6,4)-SWCNTs).*

Moreover, Raman spectra were acquired before and after (6,4)-SWCNT separation (***Figure S3***) and the intensity ratios of Raman G/D bands were calculated, which are generally used to monitor covalent sidewall reactions in SWCNTs and are thus a measure of the defect number on the SWCNT surface.[71] The results indicate a lower defect ratio after SWCNT purification (increase from 15.1 to 18.3) due to the sorting out of impurities.

Since it is known that additional separation steps lead to stronger interfacial trapping of SWCNTs between the dextran and PEG phase[64,65], the extraction yield between the two- and one-step separation was calculated and compared. For this purpose, the absorption spectra are additionally shown rescaled in ***Figure S2*** a – f (right axis), so that the different volumes of the

two separation phases and dilutions during absorption measurements were quantitatively considered. While in the two-step separation about 10.8% of all (6,4)-SWCNTs remained in the bottom phase without metallic separation and thus were accessible for (6,4)-SWCNT separation, 70.9% migrated to the top phase, and 18.3% of the non-extractable (6,4)-SWCNT were lost in the interfacial layer. After the second separation step, approximately half of the 10.8% (6,4)-SWCNTs got lost in the bottom phase, so that the extraction yield was calculated as 5.1%. Reduction to a one-step separation approach resulted in a direct effect on the yield of extractable (6,4)-SWCNTs with an increase from 5.1% to 7.4% (***Figure S2*** g). A precise understanding of these interfacial losses would be necessary for further improvement of the extraction yield. E.g. it has been shown that the molecular weight of the commonly used 6 kDa PEG/70 kDa dextran ATPE system can be changed, which also affects interfacial trapping.[72,73] However, this one-step ATPE can be scaled up to extract (6,4)-SWCNTs easily, quickly, and inexpensively on a large scale (***Figure 2*** a, ***Figure S4***). Furthermore, the remaining SWCNTs in the top phase could be recycled. This was demonstrated by precipitation, washing, and filtering of the SWCNTs in the ATPE top phase to remove the surfactant shell surrounding the SWCNTs and then drying them, which provided the SWCNT material for other sensing or ATPE experiments (***Figure S5***). Here, we showed the redispersion of these SWCNTs in 1% DOC, using a superacid-surfactant exchange based on previous literature[74], avoiding further SWCNT shortening by tip-sonication.

### 2.2. Comparison of detection efficiency

The use of NIR fluorophores for biomedical imaging is a steadily growing trend due to advantages such as lower scattering and autofluorescence of biological samples leading to higher signal-to-background ratios (SBR). While NIR imaging has long been limited to the so-called NIR-I window (700 – 900 nm), the discovery of new NIR-II (1000 – 1700 nm) fluorophores and improvements on the detector side are now extending imaging to the NIR-II

window, which is expected to further improve the SBR due to further reduced scattering and autofluorescence in this wavelength range.[35] However, the detector side must also be considered, and for NIR-II imaging, InGaAs cameras must inevitably be used. Even though their performance has improved in recent years, Si cameras are still the best-developed and are superior in all aspects such as quantum efficiency, resolution and noise (dark current).

In a first step we developed a simulation, considering the parameters of fluorophores and biological samples based on a specific biological scenario and typical parameters on the detector side (InGaAs vs Si camera). This helped us to choose the right fluorophore wavelength for a desired application. In our scenario, SWCNTs are present in solution and it is assumed that their fluorescence can be selected arbitrarily in wavelength, while retaining their advantage of a large stokes shift between excitation and emission, largely preventing the excitation light from passing through the filters to the detector. Furthermore, components of a standard microscope such as the typical wavelength-dependent power density of an LED for excitation, wavelength-dependent transmission curves of necessary optics, as well as optical interference factors such as the dark current of the detectors as well as autofluorescence and absorption of biological samples were considered (***Figure S6***). Here, the scenario is focused on imaging cells in phosphate-buffered saline (PBS) buffer as we will show experimentally in the further course. Detailed assumptions and calculations can be found in the Supporting Information (***Table S1***).

For comparison, the respective SBR of the two camera types when imaging cells in PBS with SWCNTs is shown (***Figure 3*** a). Here, the wavelength refers to the peak wavelength of SWCNTs. For Si cameras, a sweet spot is obtained at about 906 nm, thus SWCNTs with (6,4)-chirality are an excellent fit. For InGaAs cameras, there is no real sweet spot since no autofluorescence was included/exists for the NIR region. In addition, the quantum efficiency increases steadily over a wide wavelength range (slightly increasing from 985 nm to 1575 nm) while the scattering from soft tissue and of other typical fluorophores present in cell cultures

decreases. The drop in SBR around 1435 nm results from the absorption of water at this position. The highest SBR occurs at about 1629 nm before the quantum efficiency of the camera drops sharply. Overall, the SBR is lower for InGaAs cameras due to the higher impact of black body radiation and dark current (***Figure S6***), which is mainly determined by the band gap of the material system used.

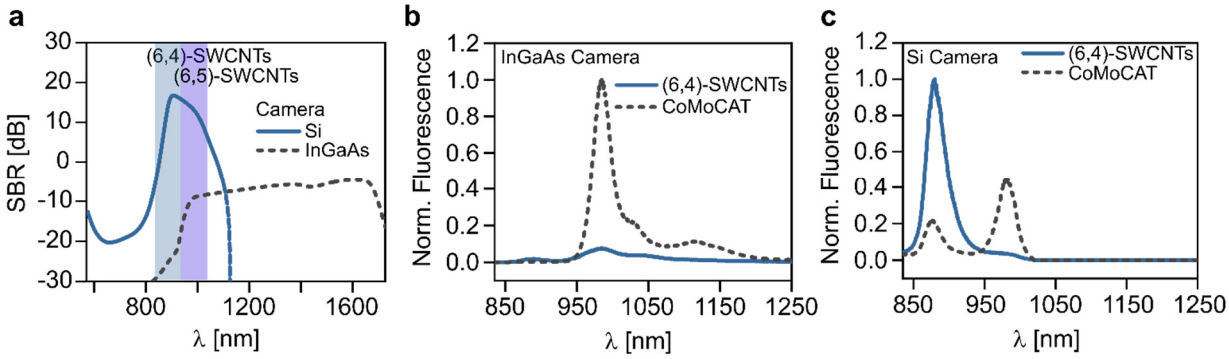


***Figure 3. Increased signals by using (6,4)-SWCNTs.*** *a) Simulation of the wavelength-dependent signal-to-background ratio (SBR) when imaging fluorophores in biological tissue in PBS using a Si or InGaAs camera. Autofluorescence of soft tissue (100 µm thickness) and typical autofluorescence from biological samples as well as absorption of water are included. The wavelength refers to the peak wavelength of SWCNTs. Highlighted areas show the main emission of (6,4)- and (6,5)-SWCNTs. b) Normalized fluorescence spectra of (6,4)-, and CoMoCAT-SWCNTs collected with an InGaAs detector weighted with the quantum efficiency of a typical InGaAs camera. Concentration was adjusted based on the area under the curve of the $E_{11}$ transitions in a range of 810 – 1350 nm. c) Normalized fluorescence spectra of the same data weighted with the quantum efficiency of a Si camera.*

However, every simulation is a specific scenario and here imaging of cells in a thin tissue like environment is mimicked. Since the background signal of Si cameras is reduced compared to InGaAs cameras, Si cameras are more sensitive to weak signals, while InGaAs cameras approach the same SBR with increasing signal strength.

To evaluate the detection efficiency of the obtained (6,4)-SWCNTs independently of the dark current of both camera systems and only based on the differences in quantum efficiency, they are compared with the parental (6,5)-enriched CoMoCAT-SWCNTs. For this purpose, their surface functionalization after ATPE was exchanged for 1% DOC and the concentration of each SWCNT material was adjusted by matching the area under the absorbance curve of the $E_{11}$ transitions in a range of 810 – 1350 nm (***Figure S7*** a, b). The wavelength-dependent fluorescence of these SWCNTs was recorded with an InGaAs detector and is shown after conversion based on the typical quantum efficiency of an InGaAs camera and a standard Si camera, normalized to the respective maximum (***Figure 3*** b, c).

For CoMoCAT-SWCNTs, which are best detected with an InGaAs camera, the (6,5)-SWCNTs emitting around 980 nm contribute to around 2/3 of the fluorescence signal with the Si camera, despite the higher sensitivity of the camera to lower wavelengths. This is based on the simplified assumption that the area under the curve can be considered a measure of signal strength. While the (6,4)-SWCNTs are barely detected by the InGaAs camera, the comparison using a Si camera shows that they appear 1.7 x brighter than CoMoCAT-SWCNTs. Although CoMoCAT-SWCNTs detected with an InGaAs detector show higher absolute intensity values (***Figure S7*** c - e), it makes detection with Si cameras using (6,4)-SWCNTs promising.

Another advantage in terms of imaging and sensing applications is the significantly higher resolution of Si cameras in relation to the absolute number of pixels (here 2048 x 2048 vs. 320 x 256 pixel). Even though higher resolution InGaAs cameras (640 x 512 pixel) are now available, this means that Si cameras have about 13-51 x higher resolution. In general, SWCNTs as nanoscale devices (dimensions 0.78 nm x 600-1000 nm) are limited by the resolution limit of optical microscopy. According to the Abbe/Rayleigh criterion, the smaller the wavelength is, the smaller the resolution limit becomes. For example, the maximum resolution for fluorescence microscopy with (6,4)-SWCNTs using a good 100x oil immersion

objective (here λ = 885 nm, NA = 1.45) is about 372 nm, which decreases with increasing wavelength (412 nm for (6,5)-SWCNTs with λ = 980 nm). Especially for imaging applications, resolution thus plays an important role, and it's not surprising that super-resolution microscopy, also with SWCNTs[75–77], is increasingly used. According to the Nyquist criterion, SWCNTs must therefore be at least 2.3 pixels apart to still be perceived as separate structures.[78] In the case of InGaAs cameras, the optical resolution limit is thus further limited due to the low pixel number. While two parallel, single (6,4)-SWCNTs at a distance of 372 nm can still be separately resolved with a typical Si camera (here 1 px ~ 65 nm at 100x magnification), this is not the case with typical InGaAs cameras (here 1 px ~ 444 nm, ***Figure 4*** a). The required pixel size would have to be at least 162 nm or smaller. Further details of the simulation can be found in the supporting information.

Since we wanted to use SWCNTs to capture the dynamics of biological processes in time and space, the next step was to evaluate the imaging quality of individual SWCNTs and how sensitive they act as dopamine sensors on the single sensor level with the two camera systems. For this purpose, SWCNTs were rendered sensitive to dopamine by exchanging the surface functionalization from surfactant to $(GT)_{10}$-ssDNA, which is known from other studies[37,58,79] to respond to dopamine with an increase in intensity (***Figure 4*** b).

Subsequently, both dopamine-responsive $(GT)_{10}$-(6,4)-SWCNTs and $(GT)_{10}$-CoMoCAT-SWCNTs were immobilized on glass and the same image section was imaged at 100x magnification in a standard microscope using both an InGaAs and Si camera. Compared to the wavelength-dependent images in ***Figure 3*** and ***Figure 4*** b, a conventional white-light LED was used for excitation instead of a specific laser, and images were acquired before and after the addition of 10 µM dopamine with an exposure time of 1 s (***Figure 4*** c, d).

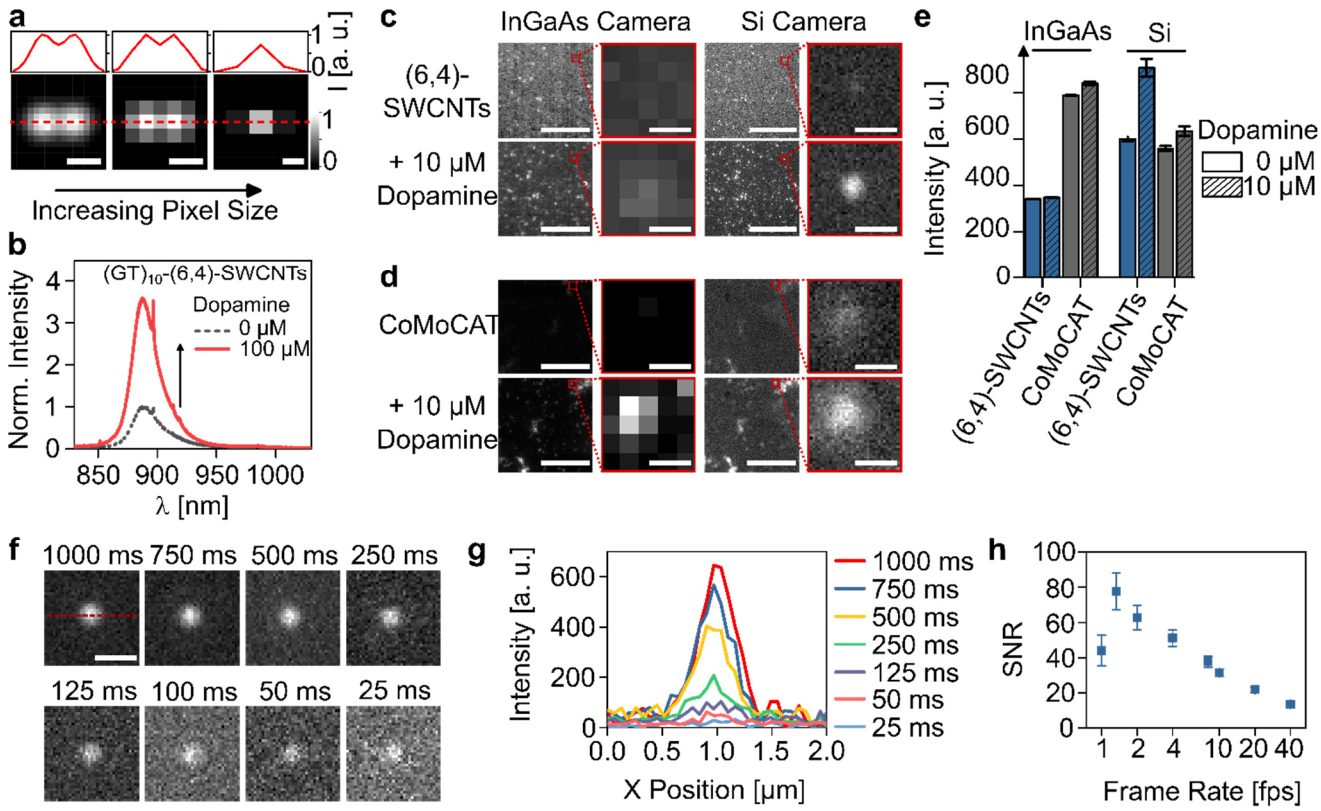


***Figure 4. Increase of sensitivity and resolution***. *a) Simulation of the camera signal of two fluorescent point sources (880 nm) whose structure sizes (diameter 100 nm) are below the resolution limit of optical microscopy. With increasing pixel size/decreasing resolution (left to right), the structures can no longer be imaged separately. From left to right with 100x objective (NA = 1.45): 65 nm (pixel size Si camera), 162 nm (theoretical Nyquist pixel size), 444 nm (pixel size InGaAs camera). Scale bars represent 400 nm. b) $(GT)_{10}$-(6,4)-SWCNTs in solution show a fluorescence increase after the addition of 100 µM dopamine. c) Comparison of the sensitivity of single $(GT)_{10}$-(6,4)- and d) $(GT)_{10}$-CoMoCAT-SWCNTs (multiple SWCNTs and one inset of a single SWCNT) immobilized on a glass surface. Fluorescence images are recorded with an InGaAs and a Si camera before and after adding 10 µM dopamine at 1 s exposure time. e) Corresponding fluorescence intensities of single SWCNTs from c) and d, mean ± SE, n = 10, f) Fluorescence images of a single $(GT)_{10}$-(6,4)-SWCNT captured with a Si camera at different exposure times. g) Corresponding height traces and h) signal-to-noise ratio (SNR) of the images in f) (mean ± SE, n = 6). Scale bars of multiple SWCNT images represent 20 µm, and of single SWCNT images represent 1 µm.*

The images show that SWCNTs are randomly arranged on the surface, but when looking at individual SWCNTs, the higher resolution of the Si camera compared to the InGaAs camera

becomes directly apparent. Comparison of absolute fluorescence brightnesses between the two camera systems must be considered cautiously because it depends on the choice of pixels to be analyzed. However, the comparison of the absolute intensities of SWCNTs before dopamine addition again shows that, based on the InGaAs camera, CoMoCAT-SWCNTs appear significantly brighter compared to (6,4)-SWCNTs and, in terms of sensitivity, show a larger intensity change after dopamine addition (6.7% increase compared to 2.1%, ***Figure 4*** e). In contrast to the previous findings (***Figure 3***) $(GT)_{10}$-(6,4)-SWCNTs appear only slightly brighter than the CoMoCAT-SWCNTs imaged with the Si camera, but show a significantly higher sensitivity for dopamine (51.3% increase instead of 13.2%). The differences in intensity comparison between the two SWCNT materials could be due to the exchanged functionalities, as ***Figure 3*** compares surfactant-dispersed SWCNTs and here ssDNA-wrapped SWCNTs are compared. In general, surfactant-dispersed SWCNTs are brighter.[80] In addition, in a previous study, it was shown that the sensor response was in some cases enhanced for monochiral sensors.[66] This may be because the exact replacement process does not appear to be identical between the different fabrication routes (direct sonication for $(GT)_{10}$-CoMoCAT-SWCNTs and functionalization exchange for $(GT)_{10}$-(6,4)-SWCNTs).[81]

Lower exposure times for $(GT)_{10}$-(6,4)-SWCNTs were tested to see how fast SWCNTs could be imaged with the Si camera (***Figure 4*** f). Down to 50 ms, single SWCNTs can be sufficiently distinguished from the background, which is also shown in the intensity traces (***Figure 4*** g). In addition, at these higher frame rates dopamine could still be detected (***Figure S8*** a). This was also possible for a second standard microscope setup (see **4. Experimental Section/Methods** for details) equipped with a Si camera that had a higher quantum efficiency in the wavelength region of interest but only a 60x objective, which is common among scientists studying cell cultures (***Figure S8*** b). Here, dopamine detection at frame rates between 4 – 10 fps was easily possible with both setups, but at higher frame rates single SWCNT traces showed higher noise.

For further quantification, we calculated the SNR based on previous literature[82,83] by taking images with and without illumination and dividing the averaged signal $Mean_{Signal}$ minus the mean noise $Mean_{Noise}$ without illumination by the standard derivation of the signal $SD_{Signal}$ (**Equation (1)**, ***Figure 4*** h).

$$SNR = \frac{Mean_{Signal} - Mean_{Noise}}{SD_{Signal}} \quad (1)$$

As the frame rate increases, the signal-to-noise ratio decreases, but still has high values > 30 at 10 fps. A similar procedure was followed with the $(GT)_{10}$-CoMoCAT-SWCNTs images with the InGaAs camera. Here, the single SWCNTs contrast was less good because of the lower resolution (***Figure S9*** a, b). In addition, although the signal-to-noise ratio showed higher values for lower frame rates compared to the imaged (6,4)-SWCNTs with the Si camera, both camera systems performed equivalently with the respective SWCNT material at high frame rates of 20 and 40 fps (***Figure S9*** c). This is probably due to the fact that the Si camera has a lower dark current, which was also evident when measuring the noise of the two camera systems, which increased for the InGaAs camera with increasing exposure time, while it remained constant for the Si camera (***Figure S8*** **d**).

Overall, the (6,4)-SWCNTs in combination with a Si camera and a standard LED for excitation are thus well-suited to keep up in performance with previous studies in which single SWCNTs were imaged with InGaAs cameras using high laser powers (~500 mW) and framerates of 10-15 fps.[36,37]

### 2.3. High-sensitivity imaging of cellular dopamine release

Finally, to test the (6,4)-SWCNT sensors in a biological application, dopamine-releasing pheochromocytoma cells (PC12) were cultured on nanosensors immobilized on glass. To improve cell adhesion, the sensor layer was additionally coated with collagen, which did not alter the sensitivity for dopamine detection (***Figure S10*** a). ***Figure 5*** a) and b) show the bright

field image of such cells and the corresponding NIR channel of fluorescent $(GT)_{10}$-(6,4)-SWCNTs.

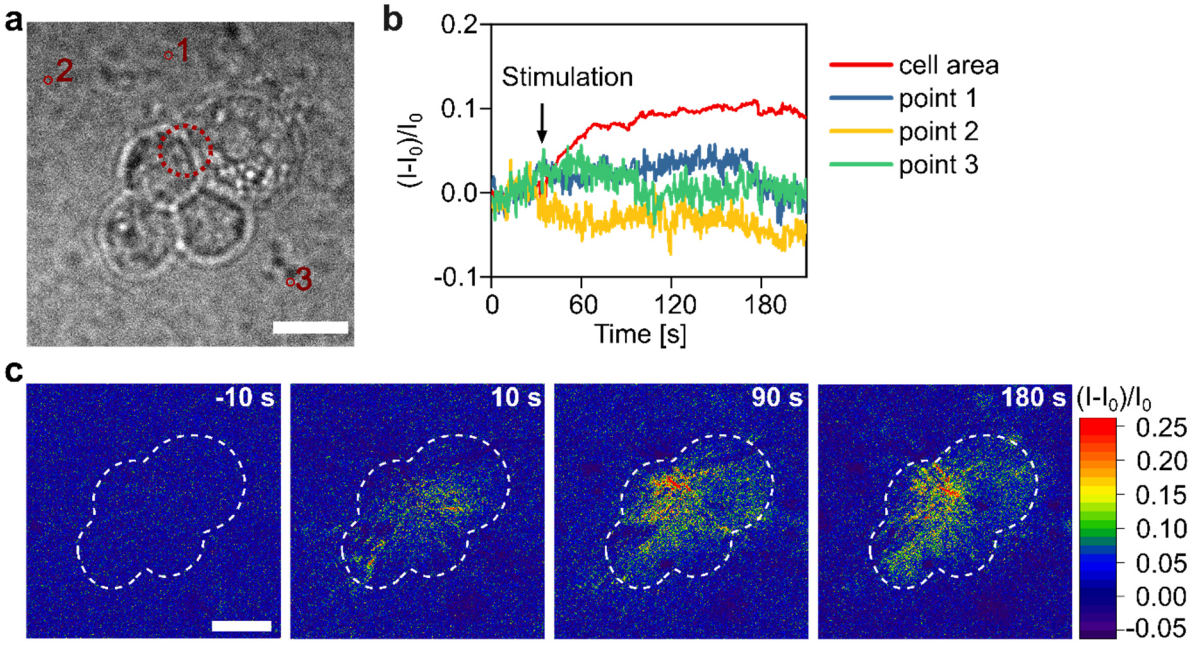


***Figure 5. Spatiotemporal imaging of dopamine release from neural progenitor cells.*** *a) Bright field image of PC12 cells cultured on glass coated with $(GT)_{10}$-SWCNTs and b) SWCNTs intensity change from ROIs (red circles in a)) during cell stimulation imaged with a Si camera. c) Color-coded normalized intensity changes at different time points show a steady increase of SWCNT fluorescence at the cell area, which indicates continued dopamine release. All scale bars represent 10 µm.*

After stimulation of cells with potassium buffer, there was an immediate increase in SWCNT fluorescence that occurred only locally at the cell surface, indicating dopamine release from cells (***Figure 5*** c, d). Here, each detector pixel was treated as a sensor to respond to the intensity changes over time. The increase in intensity occurred over several minutes, which can be attributed to continuous dopamine release. Such temporal dopamine release is also consistent with amperometric measurements, in which the release lasted for approximately three minutes[84] or continued for several minutes with subsequent stimuli.[85,86] Moreover, a control experiment in which the same stimulus was added to the sensors without cell cultivation showed

no signal change in the sensors (***Figure S10*** b), suggesting triggered dopamine release by dopaminergic PC12 cells.

## 3. Conclusion

In summary, we tailored NIR fluorescent nanosensors for optimized imaging and sensing applications with Si cameras. The simple and fast protocol for separating large amounts of monochiral (6,4)-SWCNTs make these SWCNTs now accessible to the broader community because they can be detected and imaged in 'normal' optical microscopes. In addition, the exemplary tailoring of SWCNTs for dopamine detection demonstrates the potential to resolve processes with high spatial and temporal resolution with increased sensitivity. This method thus makes SWCNTs accessible as NIR building blocks for sensors and labels for the entire field of (bio)imaging.

## 4. Experimental Section/Methods

All materials were purchased from Sigma-Aldrich unless specified otherwise.

*SWCNT Surface Modification*

Surface modification of (6,5) chirality-enriched CoMoCAT- (Sigma-Aldrich, product no. 773735) with 1% DOC was performed by mixing 1 ml of SWNCTs (4 mg·ml$^{-1}$ in DI water) with 1 ml of aqueous 2% m/m DOC. This mixture was tip sonicated in an ice bath (36 W output power – 25 min at 30% amplitude, Fisherbrand Model 120 Sonic Dismembrator) and centrifuged (2 × 30 min, 16100 g, 4 °C) to remove aggregates. The supernatant yielded homogenously dispersed 1% DOC-SWCNTs for further experiments.

For surface modification of CoMoCAT-SWCNTs with $(GT)_{10}$-ssDNA, a recently published protocol was used.[87] 100 µl of SWCNTs (2 mg·ml$^{-1}$ in PBS) were mixed with 100 µl ssDNA (2 mg/ml in PBS), followed by tip sonication (ice bath, 10 min at 30% amplitude) and centrifugation (2 × 30 min, 16100 g, 4 °C).

For recycling of SWCNTs after ATPE, SWCNTs were precipitated with methanol, washed with isopropanol and water, and filtered. After drying overnight (oven, 40 °C), SWCNTs were

collected and represented the SWCNT material for further experiments. SWCNTs were resuspended in 1% DOC with superacid-surfactant exchange based on previous literature.[74] In short, SWCNTs were dissolved in chlorosulfonic acid at a concentration of ~0.5 mg·ml$^{-1}$. Droplets of 10 µl each were added to an aqueous solution of 0.5 M NaOH and 1 wt/v% DOC until the pH reached a value of 11.

*SWCNT Separation*

Separation of (6,4)-SWCNTs was based on a modified ATPE protocol by Li et al.[65] To find the optimal parameters, SWCNTs were separated in a two-phase aqueous system containing the polymers PEG (MW 6 kDa, 8% m/v) and dextran (Carl Roth, MW 70 kDa, 4% m/v) and the surfactants DOC (0.025% m/v), SDS (0.5% m/m) and SC (varying from 0.5% to 0.9% m/m in 0.1% steps), with DOC added *via* CoMoCAT-SWCNTs dispersed in 1% DOC. A certain volume of HCl (0.5 M) was added for pH-driven separation (here: 110 µl – 190 µl in 20 µl steps for an 8 ml batch). After addition of all chemicals, the mixture was homogeneously mixed for 60 s and phase separation was accelerated by subsequent centrifugation (30 min at 3046 g, 20 °C).

After finding the optimal SC concentration, (6,4)-SWCNTs were separated from all other semiconducting and metallic chiralities in a one-step approach by simultaneously adding a certain volume of HCl and NaClO (Honeywell) with 10-15% available chlorine for pH-driven and electronic separation (here: 750 µl of 0.5 M HCl and 170 µl NaClO for a 40 ml batch, resulting in a pH of 5.9 for the bottom phase). The final bottom phase yielded monochiral (6,4)-SWCNTs.

For characterization of the resulting bottom and top phases, absorption spectra were recorded with a corresponding mimic (without SWCNTs) for baseline subtraction. For better comparison, spectra were subsequently background corrected in the form of $Ae^{-b\lambda}$ based on previous literature.[88,89] The purity was calculated by fitting the respective SWCNT $E_{11}$ chirality peaks under the absorbance curve from each ATPE phase and dividing the area of the (6,4)-SWCNT peak by the total area of all peaks. The extraction yield was calculated by determining the concentration of (6,4)-SWCNTs in the respective ATPE phase. This was calculated based on a previously published method.[87,90–92]

The bottom phase was dialyzed against 1% DOC for at least three days (300 kDa dialysis bag, Spectra/Por Spectrum Labs). The 1% DOC solution was renewed daily to replace the residual dextran with DOC and obtain a stable 1% DOC-(6,4)-SWCNT solution.

*Monochiral SWCNT Surface Exchange to ssDNA*

Exchange of 1% DOC-(6,4)-SWCNT to ssDNA-(6,4)-SWCNTs was based on kinetic exchange *via* dialysis. Purified (6,4)-SWCNTs were concentrated to an absorbance of 2.0 at the $E_{11}$ transition (880 nm) using molecular weight cut-off centrifugal filters (Amicon Ultra-15, 30 kDa). 1 ml of these SWCNTs was mixed with 100 µl of ssDNA ($(GT)_{10}$, 2 $mg \cdot ml^{-1}$ in PBS) and dialyzed against 1x PBS for three days (1 kDa dialysis bag, Spectra/Por Spectrum Labs). 1x PBS was renewed daily. After completion of dialysis, the solution within the dialysis bag was centrifuged (15 min at 16100 g). The supernatant yielded the material for further experiments.

*NIR Spectroscopy*

Absorption spectra for the characterization of SWCNT samples were recorded using a JASCO V-780-ST spectrophotometer in the wavelength range of 400 – 1350 nm in 0.5 nm steps in quartz cuvettes (Hellma, 10 mm optical path).

2D NIR fluorescence spectra were recorded with 10 s integration time using a spectrometer (Shamrock 193i, Andor Technology Ltd.) connected to a microscope (Olympus IX73). A lamp (LSE341, LOT-Quantum Design) was used in combination with a monochromator (MSH-150, LOT-Quantum Design) for excitation in the range of 400 – 700 nm in 5 nm steps.

*Raman Spectroscopy*

Raman and dopamine response fluorescence measurements were carried out using a confocal Raman microscope (inVia InSpect from Renishaw) at an excitation of 532 nm (10 mW laser power) with an integration time between 10 – 60 s. For dopamine response measurements in solution, 2 µl of a freshly prepared dopamine solution (dopamine hydrochloride in 1x PBS) was added to 200 µl of $(GT)_{10}$-(6,4)-SWCNTs in a 96-well plate, resulting in a concentration of 100 µM dopamine.

*SWCNT immobilization for single SWCNT imaging*

Glass bottom Petri dishes (Ibidi) were treated with oxygen plasma (Atto B, Diener electronic, 0.6 mbar) for 20 s. Directly after plasma cleaning, surfaces were coated with 300 µl of an APTES solution (1 wt % APTES/$H_2O$ in ethanol) and incubated for 1 hour at room temperature. Petri dishes were washed with ethanol and subsequently $H_2O$ and dried with $N_2$. 150 µl of a 0.1 nM SWCNT solution was added and incubated overnight at 4 °C. To remove non-immobilized SWCNTs the surface was rinsed three times with 1x PBS.

*Imaging of Single SWCNTs*

SWCNTs were imaged in two different setups. The first setup consisted of an inverted microscope (Nikon Eclipse Ti2) equipped with a 100x objective (CFI Plan Apochromat Lambda D 100x Oil/1.45/0.13). A white LED (CoolLED pE300 Lite, 100% power) was used in combination with a 560 ± 40 nm bandpass filter for the excitation of SWCNTs *via* the $E_{22}$ transitions. Excitation light was eliminated from emission *via* an 840 nm long-pass filter. The NIR fluorescence was imaged either with a Si camera (Hamamatsu Orca Flash 4.0) with 2048 x 2048 pixels or an InGaAs camera (Xeva 1.7 320 TE3 USB 100 Xenics) with 320 x 256 pixels, cooled down to 190 K.

The second setup consisted of an inverted microscope (Nikon Eclipse Ti2) equipped with a 60x objective (CFI P-Apo 60x Lambda Oil/1.40/0.13). A green LED emitting at 555 nm (Lumencor Spectrax Chroma, six independently controllable light sources, 100% power) was used in combination with a 550 ± 49 nm bandpass filter for SWCNT excitation. Excitation light was eliminated from emission *via* a bandpass filter in the range of 785 – 1000 nm. The NIR fluorescence was imaged with a Si camera (Hamamatsu Orca Fusion BT) with 2304 x 2304 pixels. For dopamine response measurements with immobilized SWCNTs, 20 µl of a freshly prepared dopamine solution (dopamine hydrochloride in 1x PBS) was added to 2 ml of PBS in the petri dish, resulting in a concentration of 10 µM dopamine.

The third setup used to perform the cell experiments consisted of an inverted microscope (Olympus IX73) equipped with a 100x objective (UPlanSApo/1.35/0.13-0.19). A 561 nm laser at 250 mW (Gem 561, Laser Quantum) was used for SWCNT excitation. Excitation light was eliminated from emission *via* a 780 nm long pass filter. The NIR fluorescence was imaged with a Si camera (PCO edge 4.2 bi) with 2048 x 2048 pixels at 500 ms exposure time.

*Cell Experiments:* PC12 cells were purchased from ATCC (CRL-1721) and cultivated according to the supplier's protocol. In short, cells were cultivated in a humidified 5% $CO_2$ atmosphere at 37 °C in T-75 flasks (Sarstedt) with a sub cultivation ratio of 1:4 every four days. Cells were grown in 16 ml RPMI-1640 medium (Thermo Fisher Scientific) supplemented with 10% heat inactivated horse serum (Thermo Fisher Scientific), 5% fetal bovine serum, 100 units·ml$^{-1}$ penicillin and 100 µg·ml$^{-1}$ streptomycin (Thermo Fisher Scientific).

For cultivation and differentiation of PC12 cells on top of SWCNT-coated glass surfaces, surfaces were incubated overnight at 4 °C with a collagen solution (Bornstein and Traub Type I) for better cell adhesion.

200,000 cells were plated on SWCNT-coated glass surfaces and incubated for 4-7 days in RPMI-1640 medium supplemented with 1% horse serum, 100 units·ml$^{-1}$ penicillin, 100 µg·ml$^{-1}$ streptomycin and 100 ng·ml$^{-1}$ nerve growth factor in a humidified 5% $CO_2$ atmosphere at 37 °C. For dopamine release experiments, the cell medium was exchanged to 1 ml 1x PBS supplemented with $MgCl_2$ and $CaCl_2$. To stimulate dopamine release, 18.68 µl of a 3 M KCl solution was added, resulting in a final concentration of 55 mM KCl.

**Acknowledgements**

This work was supported by the Fraunhofer Internal Programs under Grant No. Attract 038-610097. Funded by the Deutsche Forschungsgemeinschaft (DFG, German Research Foundation) under Germany´s Excellence Strategy – EXC 2033 – 390677874 – RESOLV. This work is supported by the „Center for Solvation Science ZEMOS“ funded by the German Federal Ministry of Education and Research BMBF and by the Ministry of Culture and Research of Nord Rhine- Westphalia Funded by the VW foundation.

**References**

[1] T. B. Kornberg, S. Roy, *Trends Cell Biol.* **2014**, *24*, 370.
[2] J. C. Rieckmann, R. Geiger, D. Hornburg, T. Wolf, K. Kveler, D. Jarrossay, F. Sallusto, S. S. Shen-Orr, A. Lanzavecchia, M. Mann, F. Meissner, *Nat. Immunol.* **2017**, *18*, 583.
[3] M. Dinarvand, S. Elizarova, J. Daniel, S. Kruss, *ChemPlusChem* **2020**, *85*, 1465.
[4] A. Yakushenko, E. Kätelhön, B. Wolfrum, *Anal. Chem.* **2013**, *85*, 5483.
[5] M. R. Post, D. Sulzer, *Cell Chem. Biol.* **2021**, *28*, 748.
[6] N. G. Gubernator, H. Zhang, R. G. W. Staal, E. V. Mosharov, D. B. Pereira, M. Yue, V. Balsanek, P. A. Vadola, B. Mukherjee, R. H. Edwards, D. Sulzer, D. Sames, *Science* **2009**, *324*, 1441.
[7] K. S. Hettie, T. E. Glass, *ACS Chem. Neurosci* **2016**, *7*, 21.
[8] J. Ackermann, J. T. Metternich, S. Herbertz, S. Kruss, *Angew. Chem., Int. Ed.* **2022**, *61*, e202112372.
[9] J. Zhang, A. A. Boghossian, P. W. Barone, A. Rwei, J.-H. Kim, D. Lin, D. A. Heller, A. J. Hilmer, N. Nair, N. F. Reuel, M. S. Strano, *J. Am. Chem. Soc.* **2011**, *133*, 567.
[10] H. Jin, D. A. Heller, M. Kalbacova, J.-H. Kim, J. Zhang, A. A. Boghossian, N. Maheshri, M. S. Strano, *Nat. Nanotechnol.* **2010**, *5*, 302.
[11] J.-H. Kim, C. R. Patra, J. R. Arkalgud, A. A. Boghossian, J. Zhang, J.-H. Han, N. F. Reuel, J.-H. Ahn, D. Mukhopadhyay, M. S. Strano, *ACS Nano* **2011**, *5*, 7848.
[12] M. Card, M. Gravely, S. Z. M Madani, D. Roxbury, *ACS Appl. Mater. Interfaces* **2021**, *13*, 31986.
[13] F. A. Mann, N. Herrmann, F. Opazo, S. Kruss, *Angew. Chem., Int. Ed.* **2020**, *59*, 17732.
[14] A. J. Gillen, A. A. Boghossian, *Front. Chem.* **2019**, *7*, 612.
[15] A. Setaro, M. Adeli, M. Glaeske, D. Przyrembel, T. Bisswanger, G. Gordeev, F. Maschietto, A. Faghani, B. Paulus, M. Weinelt, R. Arenal, R. Haag, S. Reich, *Nat. Commun.* **2017**, *8*, 14281.
[16] A. Spreinat, M. M. Dohmen, J. Lüttgens, N. Herrmann, L. F. Klepzig, R. Nißler, S. Weber, F. A. Mann, J. Lauth, S. Kruss, *J. Phys. Chem. C* **2021**, *125*, 18341.

[17] P. Bilalis, D. Katsigiannopoulos, A. Avgeropoulos, G. Sakellariou, *RSC Adv.* **2014**, *4*, 2911.
[18] K. Huth, M. Glaeske, K. Achazi, G. Gordeev, S. Kumar, R. Arenal, S. K. Sharma, M. Adeli, A. Setaro, S. Reich, R. Haag, *Small* **2018**, *14*, e1800796.
[19] A. Antonucci, M. Reggente, C. Roullier, A. J. Gillen, N. Schuergers, V. Zubkovs, B. P. Lambert, M. Mouhib, E. Carata, L. Dini, A. A. Boghossian, *Nat. Nanotechnol.* **2022**, *17*, 1111.
[20] H. Wu, R. Nißler, V. Morris, N. Herrmann, P. Hu, S.-J. Jeon, S. Kruss, J. P. Giraldo, *Nano Lett.* **2020**, *20*, 2432.
[21] T. T. S. Lew, V. B. Koman, K. S. Silmore, J. S. Seo, P. Gordiichuk, S.-Y. Kwak, M. Park, M. C.-Y. Ang, D. T. Khong, M. A. Lee, M. B. Chan-Park, N.-H. Chua, M. S. Strano, *Nat. Plants* **2020**, *6*, 404.
[22] J. P. Giraldo, M. P. Landry, S.-Y. Kwak, R. M. Jain, M. H. Wong, N. M. Iverson, M. Ben-Naim, M. S. Strano, *Small* **2015**, *11*, 3973.
[23] J. Meier, J. Stapleton, E. Hofferber, A. Haworth, S. Kachman, N. M. Iverson, *Nanomaterials* **2021**, *11*, 243.
[24] D. A. Heller, G. W. Pratt, J. Zhang, N. Nair, A. J. Hansborough, A. A. Boghossian, N. F. Reuel, P. W. Barone, M. S. Strano, *Proc. Natl. Acad. Sci. U. S. A.* **2011**, *108*, 8544.
[25] M. H. Wong, J. P. Giraldo, S.-Y. Kwak, V. B. Koman, R. Sinclair, T. T. S. Lew, G. Bisker, P. Liu, M. S. Strano, *Nat. Mater.* **2017**, *16*, 264.
[26] S. Kruss, M. P. Landry, E. Vander Ende, B. M. A. Lima, N. F. Reuel, J. Zhang, J. Nelson, B. Mu, A. Hilmer, M. Strano, *J. Am. Chem. Soc.* **2014**, *136*, 713.
[27] S. Jeong, D. Yang, A. G. Beyene, J. T. Del Bonis-O'Donnell, A. M. M. Gest, N. Navarro, X. Sun, M. P. Landry, *Sci. Adv.* **2019**, *5*, eaay3771.
[28] G. Bisker, J. Dong, H. D. Park, N. M. Iverson, J. Ahn, J. T. Nelson, M. P. Landry, S. Kruss, M. S. Strano, *Nat. Commun.* **2016**, *7*, 10241.
[29] R. Ehrlich, A. Hendler-Neumark, V. Wulf, D. Amir, G. Bisker, *Small* **2021**, *17*, e2101660.
[30] R. M. Williams, C. Lee, D. A. Heller, *ACS Sens.* **2018**, *3*, 1838.
[31] V. Zubkovs, N. Schuergers, B. Lambert, E. Ahunbay, A. A. Boghossian, *Small* **2017**, *13*, 1701654.
[32] S. Agarwal, N. E. Kallmyer, D. X. Vang, A. V. Ramirez, M. M. Islam, A. C. Hillier, L. J. Halverson, N. F. Reuel, *Anal. Chem.* **2022**, *94*, 856.
[33] R. Nißler, O. Bader, M. Dohmen, S. G. Walter, C. Noll, G. Selvaggio, U. Groß, S. Kruss, *Nat. Commun.* **2020**, *11*, 5995.
[34] M. J. O'Connell, S. M. Bachilo, C. B. Huffman, V. C. Moore, M. S. Strano, E. H. Haroz, K. L. Rialon, P. J. Boul, W. H. Noon, C. Kittrell, J. Ma, R. H. Hauge, R. B. Weisman, R. E. Smalley, *Science* **2002**, *297*, 593.
[35] G. Hong, A. L. Antaris, H. Dai, *Nat. Biomed. Eng.* **2017**, *1*, 0010.
[36] S. Kruss, D. P. Salem, L. Vuković, B. Lima, E. Vander Ende, E. S. Boyden, M. S. Strano, *Proc. Natl. Acad. Sci. U. S. A.* **2017**, *114*, 1789.
[37] S. Elizarova, A. A. Chouaib, A. Shaib, B. Hill, F. Mann, N. Brose, S. Kruss, J. A. Daniel, *Proc. Natl. Acad. Sci. U. S. A.* **2022**, *119*, e2202842119.
[38] A. G. Beyene, K. Delevich, J. T. Del Bonis-O'Donnell, D. J. Piekarski, W. C. Lin, A. W. Thomas, S. J. Yang, P. Kosillo, D. Yang, G. S. Prounis, L. Wilbrecht, M. P. Landry, *Sci. Adv.* **2019**, *5*, eaaw3108.
[39] M. Dinarvand, E. Neubert, D. Meyer, G. Selvaggio, F. A. Mann, L. Erpenbeck, S. Kruss, *Nano Lett.* **2019**, *19*, 6604.
[40] R. Guntupalli, R. Allen, in *Infrared and Photoelectronic Imagers and Detector Devices II* (Eds.: R. E. Longshore, A. Sood), Proc. SPIE **2006**, p. 629401.
[41] A. M. Smith, M. C. Mancini, S. Nie, *Nat. Nanotechnol.* **2009**, *4*, 710.

[42] B. Song, B. Shi, S. T. Suran-Brunelli, S. Zhu, J. Klamkin, *IEEE J. Sel. Top. Quantum Electron.* **2022**, *28*, 1.
[43] S. M. Bachilo, M. S. Strano, C. Kittrell, R. H. Hauge, R. E. Smalley, R. B. Weisman, *Science* **2002**, *298*, 2361.
[44] F. Yang, M. Wang, D. Zhang, J. Yang, M. Zheng, Y. Li, *Chem. Rev.* **2020**, *120*, 2693.
[45] M. He, A. I. Chernov, P. V. Fedotov, E. D. Obraztsova, J. Sainio, E. Rikkinen, H. Jiang, Z. Zhu, Y. Tian, E. I. Kauppinen, M. Niemelä, A. O. I. Krause, *J. Am. Chem. Soc.* **2010**, *132*, 13994.
[46] H. An, A. Kumamoto, H. Takezaki, S. Ohyama, Y. Qian, T. Inoue, Y. Ikuhara, S. Chiashi, R. Xiang, S. Maruyama, *Nanoscale* **2016**, *8*, 14523.
[47] F. Yang, X. Wang, D. Zhang, J. Yang, Da Luo, Z. Xu, J. Wei, J.-Q. Wang, Z. Xu, F. Peng, X. Li, R. Li, Y. Li, M. Li, X. Bai, F. Ding, Y. Li, *Nature* **2014**, *510*, 522.
[48] V. Shumeiko, Y. Paltiel, G. Bisker, Z. Hayouka, O. Shoseyov, *Biosens. Bioelectron.* **2021**, *172*, 112763.
[49] V. Shumeiko, E. Malach, Y. Helman, Y. Paltiel, G. Bisker, Z. Hayouka, O. Shoseyov, *Sens. Actuators, B* **2021**, *327*, 128832.
[50] X. Wei, T. Tanaka, S. Li, M. Tsuzuki, G. Wang, Z. Yao, L. Li, Y. Yomogida, A. Hirano, H. Liu, H. Kataura, *Nano Lett.* **2020**, *20*, 410.
[51] B. Xu, T. Kaneko, Y. Shibuta, T. Kato, *Sci. Rep.* **2017**, *7*, 11149.
[52] R. Nißler, J. Ackermann, C. Ma, S. Kruss, *Anal. Chem.* **2022**, *94*, 9941.
[53] S. Ghosh, S. M. Bachilo, R. B. Weisman, *Nat. Nanotechnol.* **2010**, *5*, 443.
[54] M. S. Arnold, A. A. Green, J. F. Hulvat, S. I. Stupp, M. C. Hersam, *Nat. Nanotechnol.* **2006**, *1*, 60.
[55] M. Zheng, A. Jagota, E. D. Semke, B. A. Diner, R. S. McLean, S. R. Lustig, R. E. Richardson, N. G. Tassi, *Nat. Mater.* **2003**, *2*, 338.
[56] B. S. Flavel, M. M. Kappes, R. Krupke, F. Hennrich, *ACS Nano* **2013**, *7*, 3557.
[57] H. Liu, D. Nishide, T. Tanaka, H. Kataura, *Nat. Commun.* **2011**, *2*, 309.
[58] R. Nißler, F. A. Mann, H. Preiß, G. Selvaggio, N. Herrmann, S. Kruss, *Nanoscale* **2019**, *11*, 11159.
[59] H. Ozawa, N. Ide, T. Fujigaya, Y. Niidome, N. Nakashima, *Chem. Lett.* **2011**, *40*, 239.
[60] A. Nish, J.-Y. Hwang, J. Doig, R. J. Nicholas, *Nat. Nanotechnol.* **2007**, *2*, 640.
[61] C. Y. Khripin, J. A. Fagan, M. Zheng, *J. Am. Chem. Soc.* **2013**, *135*, 6822.
[62] J. A. Fagan, C. Y. Khripin, C. A. Silvera Batista, J. R. Simpson, E. H. Hároz, A. R. Hight Walker, M. Zheng, *Adv. Mater.* **2014**, *26*, 2800.
[63] M. Iqbal, Y. Tao, S. Xie, Y. Zhu, D. Chen, X. Wang, L. Huang, D. Peng, A. Sattar, M. A. B. Shabbir, H. I. Hussain, S. Ahmed, Z. Yuan, *Biol. Proced. Online* **2016**, *18*, 18.
[64] N. K. Subbaiyan, S. Cambré, A. N. G. Parra-Vasquez, E. H. Hároz, S. K. Doorn, J. G. Duque, *ACS Nano* **2014**, *8*, 1619.
[65] H. Li, G. Gordeev, O. Garrity, S. Reich, B. S. Flavel, *ACS Nano* **2019**, *13*, 2567.
[66] R. Nißler, L. Kurth, H. Li, A. Spreinat, I. Kuhlemann, B. S. Flavel, S. Kruss, *Anal. Chem.* **2021**, *93*, 6446.
[67] A. L. Antaris, O. K. Yaghi, G. Hong, S. Diao, B. Zhang, J. Yang, L. Chew, H. Dai, *Small* **2015**, *11*, 6325.
[68] J. K. Streit, J. A. Fagan, M. Zheng, *Anal. Chem.* **2017**, *89*, 10496.
[69] J. L. Blackburn, J. M. Holt, V. M. Irurzun, D. E. Resasco, G. Rumbles, *Nano Lett.* **2012**, *12*, 1398.
[70] W. Zhou, D. Nakamura, H. Liu, H. Kataura, S. Takeyama, *Sci. Rep.* **2014**, *4*, 6999.
[71] M. S. Dresselhaus, G. Dresselhaus, R. Saito, A. Jorio, *Phys. Rep.* **2005**, *409*, 47.
[72] M. Lyu, B. Meany, J. Yang, Y. Li, M. Zheng, *J. Am. Chem. Soc.* **2019**, *141*, 20177.
[73] C. M. Sims, J. A. Fagan, *Carbon* **2022**, *191*, 215.

[74] P. Wang, M. Kim, Z. Peng, C.-F. Sun, J. Mok, A. Lieberman, Y. Wang, *ACS Nano* **2017**, *11*, 9231.
[75] S. Nandi, K. Caicedo, L. Cognet, *Nanomaterials* **2022**, *12*, 1433.
[76] B. Kagan, A. Hendler-Neumark, V. Wulf, D. Kamber, R. Ehrlich, G. Bisker, *Adv. Photonics Res.* **2022**, *3*, 2200244.
[77] K. Otsuka, A. Ishii, Y. K. Kato, *Opt. Express* **2019**, *27*, 17463.
[78] A. Ehrmann, T. Blachowicz, in *Examination of Textiles with Mathematical and Physical Methods* (Eds.: A. Ehrmann, T. Blachowicz), Springer International Publishing. Cham **2017**, p. 55.
[79] F. A. Mann, N. Herrmann, D. Meyer, S. Kruss, *Sensors* **2017**, *17*, 1521.
[80] J. G. Duque, L. Oudjedi, J. J. Crochet, S. Tretiak, B. Lounis, S. K. Doorn, L. Cognet, *J. Am. Chem. Soc.* **2013**, *135*, 3379.
[81] Y. Yang, A. Sharma, G. Noetinger, M. Zheng, A. Jagota, *J. Phys. Chem. C* **2020**, *124*, 9045.
[82] J. Lu, B. Gu, X. Wang, Y. Zhang, *PLoS One* **2017**, *12*, e0169358.
[83] K. V. Vienola, M. Damodaran, B. Braaf, K. A. Vermeer, J. F. de Boer, *Opt. Lett.* **2015**, *40*, 5335.
[84] H.-F. Cui, J.-S. Ye, Y. Chen, S.-C. Chong, F.-S. Sheu, *Anal. Chem.* **2006**, *78*, 6347.
[85] K. D. Kozminski, D. A. Gutman, V. Davila, D. Sulzer, A. G. Ewing, *Anal. Chem.* **1998**, *70*, 3123.
[86] B. Zhang, K. L. Adams, S. J. Luber, D. J. Eves, M. L. Heien, A. G. Ewing, *Anal. Chem.* **2008**, *80*, 1394.
[87] R. Nißler, F. A. Mann, P. Chaturvedi, J. Horlebein, D. Meyer, L. Vuković, S. Kruss, *J. Phys. Chem. C* **2019**, *123*, 4837.
[88] A. V. Naumov, S. Ghosh, D. A. Tsyboulski, S. M. Bachilo, R. B. Weisman, *ACS Nano* **2011**, *5*, 1639.
[89] M. Pfohl, D. D. Tune, A. Graf, J. Zaumseil, R. Krupke, B. S. Flavel, *ACS Omega* **2017**, *2*, 1163.
[90] F. Schöppler, C. Mann, T. C. Hain, F. M. Neubauer, G. Privitera, F. Bonaccorso, D. Chu, A. C. Ferrari, T. Hertel, *J. Phys. Chem. C* **2011**, *115*, 14682.
[91] J. K. Streit, S. M. Bachilo, S. Ghosh, C.-W. Lin, R. B. Weisman, *Nano Lett.* **2014**, *14*, 1530.
[92] S. R. Sanchez, S. M. Bachilo, Y. Kadria-Vili, C.-W. Lin, R. B. Weisman, *Nano Lett.* **2016**, *16*, 6903.
[93] G. de Miguel, G. Vicidomini, B. Harke, A. Diaspro, in *Micro and Nano Technologies, Three-Dimensional Microfabrication Using Two-photon Polymerization* (Ed.: Tommaso Baldacchini), William Andrew Publishing **2016**, p. 190.

J. Ackermann, J. Stegemann, T. Smola, E. Reger, S. Jung, A. Schmitz, S. Herbertz, L. Erpenbeck, K. Seidl, S. Kruss *

High sensitivity near-infrared imaging of fluorescent nanosensors


(6,4)-SWCNTs fluoresce in the near-infrared (880 nm) and can be chemically functionalized with DNA to act as sensors. They provide access to the sweet spot between the efficiency of (Si) cameras of standard microscope equipment and the advantages of the near-infrared, which is shown by high-resolution mapping of dopamine release from cells.